# Attractive and Repulsive Interactions Originating from Lateral Nanometer Variations in Surface Charge/Energy of Hyaluronic Acid and Chondroitin Sulfate Doped Polypyrrole Observed Using Atomic Force Microscopy

A. Gelmi, M. J. Higgins,* and G. G. Wallace*

ARC Centre of Excellence for Electromaterials Science, Intelligent Polymer Research Institute, AIIM Facility, Innovation Campus, University of Wollongong, North Wollongong, New South Wales, 2500, Australia

Ⓢ *Supporting Information*

ABSTRACT: Phase imaging in atomic force microscopy (AFM) is a useful technique for determining dissipative tip−sample interactions related to changes in the material surface properties such as local stiffness or adhesion. In this work, we applied both phase imaging and phase spectroscopy measurements to conducting polymer (polypyrrole) doped with either hyaluronic acid or chondroitin sulfate. As observed in previous studies, phase-separated regions correlating with the characteristic nodular topography of polypyrrole and attributed to crystalline (doped) and amorphous (undoped) regions were observed. However, through additional phase spectroscopy measurements, we show that the phase-separated regions can arise due to variation in attractive and repulsive tip−sample interactions across the polymer surface. We show that these attractive and repulsive interactions are dependent on the redox state and degree of doping and suggest that they are related to phase separation of the polymer surface charge and/or energy. The latter may have implications for these materials when under investigation in a fluid, or biological, environment. For example, such surface variations will play a role in electrostatic forces, which in turn can influence protein and cellular interactions.
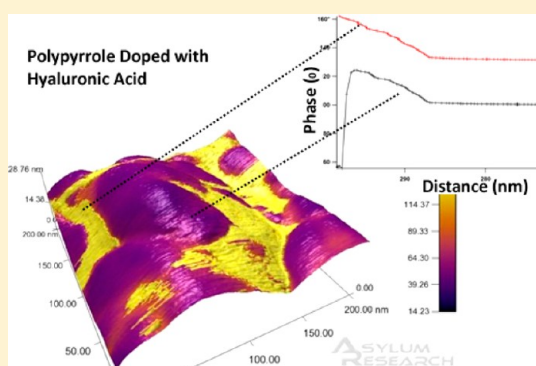
INTRODUCTION

Polypyrrole (PPy) is an organic conducting polymer (OCP) widely researched as a biomaterial for tissue regeneration and engineering applications.[1,2] Coupled with their unique mechanisms of transmitting electrical signals, the seemingly inherent compatibility of carbon-based OCP's with biological building blocks of similar composition (e.g., DNA and proteins) offers several advantages when considering their use as implantable electrodes,[3] conductive scaffolds,[4] or biosensors.[5,6] They are also softer than traditional metal electrodes and therefore perceived as suitable materials in the effort to bridge hard-wired electronics with soft biological systems.[7] A characteristic feature of OCPs is their ability to incorporate biomolecules into the polymer (termed doping) to create a conductive biomaterial. The process of doping generally occurs during the synthesis of the polymer.[5] Oxidation of the monomer results in polymerization to produce a conjugated polymer chain with positive charges along its length. Anionic molecules in the growth electrolyte are then incorporated to balance the charge on the polymer chain backbone (see Figure 1a).

Biological anionic molecules are commonly incorporated to improve biocompatibility or target specific cellular function.[8−10] Garner et al.[8] incorporated heparin, an anticoagulant
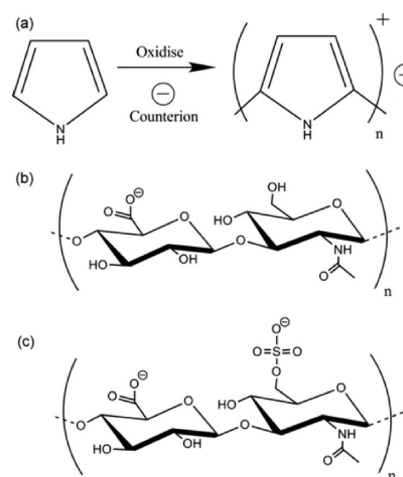

Figure 1. (a) Oxidation of pyrrole monomer in the presence of a counteranion, (b) hyaluronic acid, and (c) chondroitin sulfate A.

polysaccharide, into PPy and demonstrated that the growth of human umbilical vein endothelial cells was supported on these materials. Many different combinations of conducting polymers and biomolecule dopants have similarly been used to assess their biocompatibility and ability to control cell growth via electrical stimulation.[11−13] However, the incorporation of biomolecules, even the likes of extracellular matrix (ECM) molecules, does not always prove beneficial. For example, Lee and Schmidt[14] showed that a polypyrrole/hyaluronic acid (PPy/HA) conjugate decreased the adhesion of human dermal fibroblasts due to the increased hydrophilicity of the surface. In previous studies using PPy/HA and PPy/chondroitin sulfate (PPy/CS), both materials supported muscle myoblast proliferation, although only PPy/CS could continue to support muscle fiber formation.[15] A corresponding study revealed that these ECM molecules and other dopants can have profound effects on the nanoscale physical properties such as topography, roughness, modulus, and actuation.[16]

The dopant chemistry influences cell−surface interactions either through direct interactions with the cell membrane or via ECM components (e.g., fibronectin, collagen) that bind cell surface receptors (e.g., integrins) to mediate cell adhesion and form part of a continuum with the cytoskeleton for cell signaling. However, little is known about the effect of doping biomolecules on the nanoscale surface chemistry of conducting polymers, particularly the possible heterogeneity in surface charge/energies or specific distribution of exposed regions of the doped biomolecule at the interface. In this study, we use dynamic mode (AC mode) atomic force microscopy (AFM) to further elucidate variations in surface properties of PPy/CS and PPy/HA substrates on a lateral nanometer scale, which is relevant to the length scale of cellular interactions. This mode of AFM is used to acquire topographical information but is also sensitive to local variations in surface properties that cause changes in the frequency, amplitude, and phase signal of the cantilever as it is oscillated during scanning across the sample. In particular, changes in the phase signal can be attributed to nondissipative and dissipative interactions between the tip and sample[17,18] and recorded simultaneously with the topography during scanning.

In the few studies using AFM phase imaging to study conducting polymers, phase-separated regions in polyaniline and cellulose acetate blends were attributed to differences in the stiffness of the two components.[19] For electrochemically polymerized polybithiophene films, AFM phase imaging has been used to study stiffness changes associated with variations in crystallinity,[20] with the view of explaining heterogeneous conductive properties in these polymers. Variations in the phase signal correlated with topography and were attributed to the presence of crystalline and amorphous areas. The nodules of the polymer films were described as being composed of higher molecular weight components with more crystallinity and higher conductivity.[21−23] However, determining the origin of phase-separated regions is often ambiguous,[24] particularly for heterogeneous materials with unknown properties. Typically a phase shift is defined through a priori knowledge of the sample (e.g., block copolymer of known constituents)[25] or through further analysis to verify the interpretation of the phase separation.[26]

In this work, we use AFM phase imaging to understand phase-separated regions in PPy films doped with HA and CS (chemical structures shown in Figure 1), which have been used previously in biocompatibility and adhesion studies for nerve,

bone, and muscle cells.[9,10,15,27,28] By correlating the topographical and phase images with a more in depth analysis of monitoring the phase signal as a function of the tip−sample separation distance (phase-separation curves), we show that phase-separated regions arise due to variations in the propensity of the tip to sample attractive and repulsive forces in different regions of the polymer. This appears to be a general phenomenon in conducting polymers, irrespective of the dopant, and holds important information for further work using these materials in fluid environments to study protein and cellular interactions.

■ EXPERIMENTAL METHODS

Reagents. The pyrrole monomer was obtained from Merck and distilled prior to use. The chemicals used as the dopants were the sodium salts of hyaluronic acid (HA) and chondroitin sulfate A (CS). CS was obtained from Sigma and HA was from Fluka. All solutions were prepared with deionized Milli-Q water (18.2 MU).

Preparation of Polymer Films. Gold-coated mylar was first prepared by cutting 1 cm^2 areas and then cleaning with ethanol and Milli-Q water. Aqueous monomer solutions were prepared for the two dopants, HA and CS. The monomer solutions of 0.2 M pyrrole and dopant were degassed in N$_2$ for 10 min prior to polymerization of the polymers. Three different dopant concentrations of 0.1, 2, and 10 mg/mL were used. PPy films were grown galvanostatically at a current density of 0.25 mA/cm^2 for 10 min in the aqueous monomer solution using an eDAQ EA161 potentiostat. Polymer growth was performed in a standard three-electrode electrochemical cell with the gold-coated mylar as the working electrode, a platinum mesh counter electrode, and Ag/AgCl reference electrode. After growth, the films were washed with Milli-Q water, gently dried with N$_2$ gas, and fixed onto glass slides until use.

Atomic Force Microscopy. The polymer films were scanned using MikroMasch NCS15/AlBS cantilevers (spring constant of ∼35 N/m) in AC mode with an MFP-3D AFM (Asylum Research, Santa Barbara, CA) to simultaneously produce topographical and phase images. The scanning was conducted in air in ambient conditions with a scan rate of 0.5 Hz and scan area of 500 nm. Imaging was compared using two different set points, a higher value of 750 mV and a lower value of 600 mV. An initial free amplitude of 0.8−0.9 V was used for both set-point values. For imaging of the films, five images were obtained from different regions of several films using a set point of 600 mV for a statistical analysis of the phase signal.

Phase Mapping and Curves. The phase-separation curves were performed using a z-distance of 500 nm, with an absolute trigger point amplitude of 600 mV and free amplitude of 0.8−0.9 V at a scan rate of 1 Hz. Phase curve mapping was performed over a scan area of 500 or 100 nm with a resolution of 32 × 32 pixels. The phase value (contrast) of each pixel represented the final phase value measured at the trigger point amplitude of 600 mV.

Phase-curve maps were performed on oxidized and reduced PPy/HA and PPy/CS polymers. Phase-curve maps were performed on the film after oxidation and then on the same film after reduction. The films were oxidized and reduced with an applied constant voltage of 500 and −500 mV, respectively, in an electrolytic solution of 0.1 M NaCl for 10 min and then washed with Milli-Q water and dried with N$_2$ prior to the measurements.
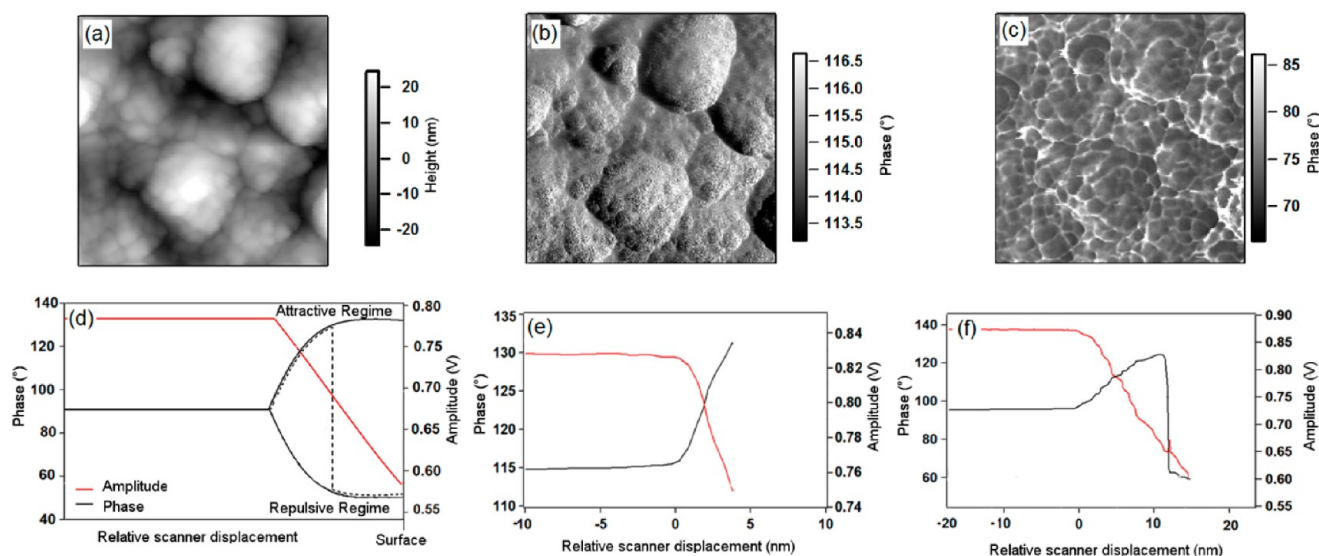
Figure 2. (a) A 500 nm topography scan of PPy/HA; phase scans over the same area, (b) 750 mV set point, and (c) 600 mV set point. (d) Phase-separation curve schematic. (e) Phase-separation curve performed on PPy/HA surface with a 750 mV trigger, and (f) phase-separation curve performed on PPy/HA surface with a 600 mV trigger. Phase (black line) amplitude (red line) signal.

Kelvin Probe Force Microscopy. Kelvin probe force microscopy (KPFM) was performed using Nanoworld EFM-20 cantilevers (spring constant of ~2.8 N/m) with a PtIr5 coating. The scanning was conducted in air in ambient conditions with a scan rate of 0.5 Hz over a scan area of 1 μm × 1 μm with a set point of 700 mV and an applied bias of 3 V on the tip.

■ RESULTS

AFM Phase Imaging of PPy/HA and PPy/CS. Parts a and b of Figure 2 show a 500 nm topographical and phase image of a PPy/HA film, respectively, measured using the higher set point of 750 mV. The typical nodular, or "cauliflower", topography is observed (Figure 2a), while the phase image (Figure 2b) displays a similar appearance. For the phase image, the delineation of the nodular topography arises from positive (lighter areas on the right edge of features) or negative (darker areas on the left edge of features) phase shifts representing very small changes of ±2°. These small phase changes are due to error in the feedback that attempts to maintain a constant tip–sample separation during imaging and are only indicative (i.e., artifact) of variations in surface topography. Figure 2c shows the same region of the film imaged with the lower set point of 600 mV. Phase-separated regions are clearly defined by the nodules displaying a more negative phase shift (darker regions), while the periphery of the nodules show a more positive phase shift (lighter areas). Imaging with this lower set point also produces significantly larger phase shifts of up to ≈60°.

Phase-Separation Curves. To understand how changes in the phase can occur, different solutions for the phase as a function of tip–sample separation are shown in a schematic diagram (Figure 2d). The corresponding amplitude signal is shown as a solid red line. When off the surface, the cantilever oscillation is unperturbed and the phase is 90° at the cantilever resonance frequency. As the tip starts to interact with the surface and causes damping of the amplitude, there are two possible solutions for the phase in conservative interactions (e.g., where the net energy dissipated from the tip is zero). For purely attractive interactions, there is a positive phase branch to 180° (attractive region). Conversely, for purely repulsive

interactions, there is a negative phase branch to 0° (repulsive region). More often in experiments an initial attractive region followed by a jump down into a repulsive region is observed (dashed line), particularly if sufficiently higher free amplitudes and lower set points are used. The jump from attractive to repulsive regions is termed bistability and may result in phase artifacts if the tip uncontrollably moves between the two regions. This is particularly the case if one is intent on observing dissipative/phase changes associated with material stiffness. The issue can be avoided by choosing a suitable set point, as determined by the phase-separation curves. Maintaining the tip in the attractive region is generally referred to being in "noncontact" while for the repulsive region the tip intermittently contacts the sample or operates in standard AC mode. A more detailed theoretical and experimental analysis of dynamic AFM modes, including details on the phase signal, has been undertaken by others.[29]

Figure 2e shows an actual phase-separation curve performed on the PPy/HA surface with a set point of 750 mV. The tip remains in the attractive region, as only a positive phase shift is observed, and generally represents the condition for the "noncontact" image in Figure 2b. In contrast, the lower set point of 600 mV produces an initial positive phase shift followed by a negative shift into the repulsive region (Figure 2f), as schematized in Figure 2d (dashed line). A lower set point of 600 mV was used throughout the remainder of the study to undertake a more in depth analysis of the phase contrast.

AFM Phase Mapping. Of interest to this study was elucidating the phase separations when operating at the lower set point, as shown in Figure 2c. This was done using phase mapping by performing an array of phase-separation curves to simultaneously provide information on the topography and corresponding spatial distribution of the phase signal (Figure 3). For these experiments, a standard AC mode phase image was initially performed (Figure 3, parts a and b) and then a phase map of a zoomed-in region (red outline) was done (Figure 3, parts e and f), which included a corresponding topographic image (Figure 3, parts c and d). We found that the phase separation (i.e., light and dark regions) in the phase maps
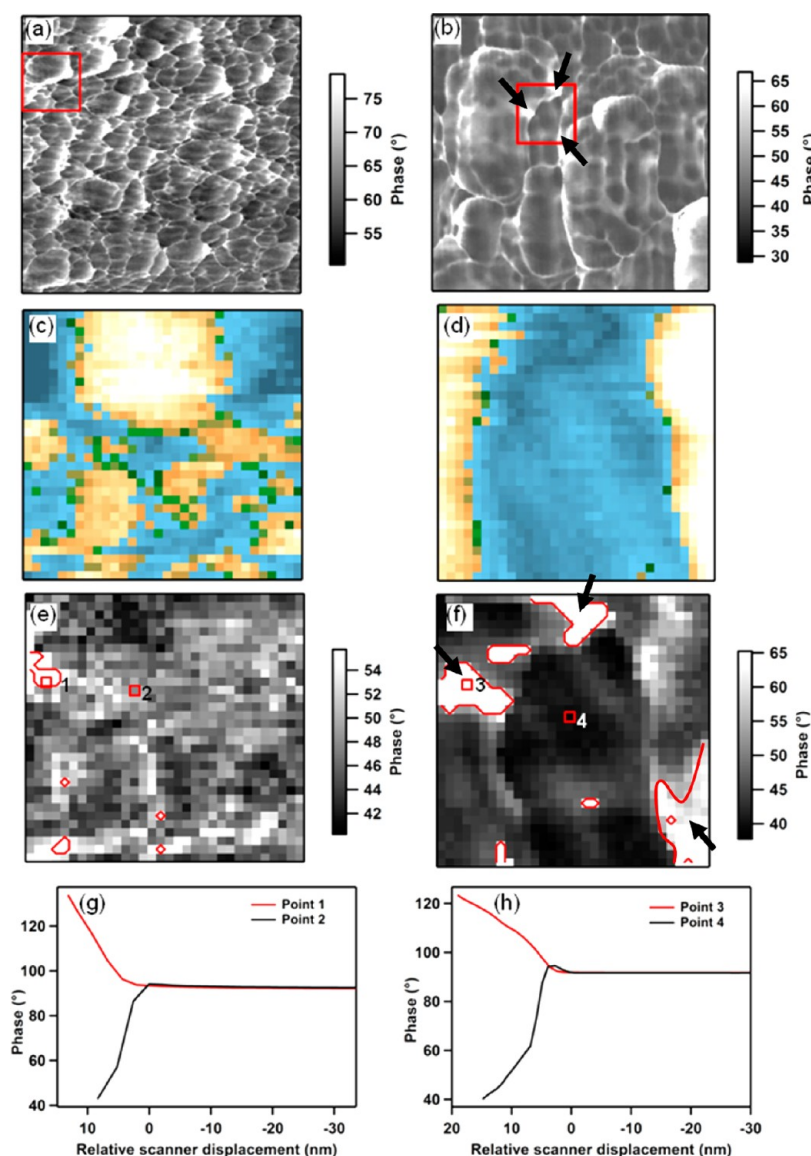
Figure 3. Images of 500 nm phase scans of (a) 2 mg/mL PPy/CS and (b) 2 mg/mL PPy/HA. Phase-curve maps of the 100 nm area marked in red showing the topography image, (c) PPy/CS and (d) PPy/HA and phase image, (e) PPy/CS and (f) PPy/HA. Individual phase curves of (g) points 1 and 2 and (h) points 3 and 4 as annotated in panels e and f. Attractive regions are outlined in red in panels e and f.

did not always correlate with their expected distribution at the nodules and nodule peripheries in the topographic image, nor did they always correlate with the phase-separated regions in the standard AC mode phase images. This appeared to be due to a number reasons: first, the phase maps and corresponding topographic image have lower lateral resolution compared to the standard AC mode imaging. This means that the phase map may not have been able to discern the same phase-separated regions, particularly those of smaller nodules that reside within larger nodules. This was particularly evident for PPy/CS whose structure was composed of nodules with smaller diameters. For example, in PPy/CS, the lighter areas of the phase map (Figure 3e, red outline) occurred more at the peripheries (blue regions) in the corresponding topographic image (Figure 3c); however, the same phase regions did not correlate strongly with the phase separation in the AC mode phase image (Figure 3a). Second, the lighter phase areas at the peripheries of smaller nodules tended to extend onto regions of surrounding higher nodules. This observation was more noticeable in smaller scan

areas of the phase maps and, thus, the correlation between phase and topography was not always clear. This is evident for PPy/HA in Figure 3f where the lighter phase regions (red outline) do not correlate clearly with the peripheries (blue regions) in the corresponding topographic image (Figure 3d), but in this case they are still identified at their equivalent positions (three black arrows) in the AC mode phase image (Figure 3b). It is also noted in that in Figure 3f where lighter regions were expected in the peripheries (Figure 3d, blue region), the latter were in fact lower-lying nodules; this highlighted the difficulty in visually recapitulating the AC mode phase image in the phase maps. Supporting Information Figure S1 shows more examples of such phase maps, with significant phase separation for both PPy/CS and PPy/HA.

As each pixel in the phase maps represents a single phase-separation curve, representative curves from light and dark areas, marked point 1 and 2 for PPy/HA and marked 3 and 4 for PPy/CS are displayed in Figure 3, parts g and f. For the lighter areas, the curves displayed only a positive shift,
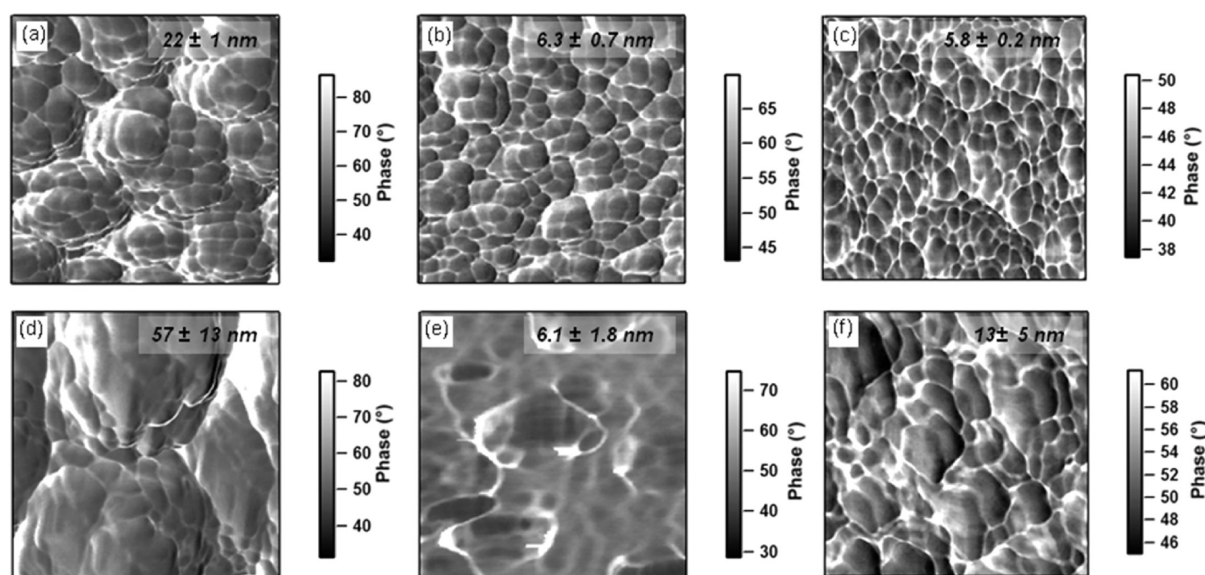
Figure 4. Representative 500 nm scan phase images with a set point of 600 mV. Average rms roughness of five scans per sample is annotated in the top right corner. PPy/CS: (a) 0.1 mg/mL, (b) 2 mg/mL, (c) 10 mg/mL. PPy/HA: (d) 0.1 mg/mL, (e) 2 mg/mL, (f) 10 mg/mL.
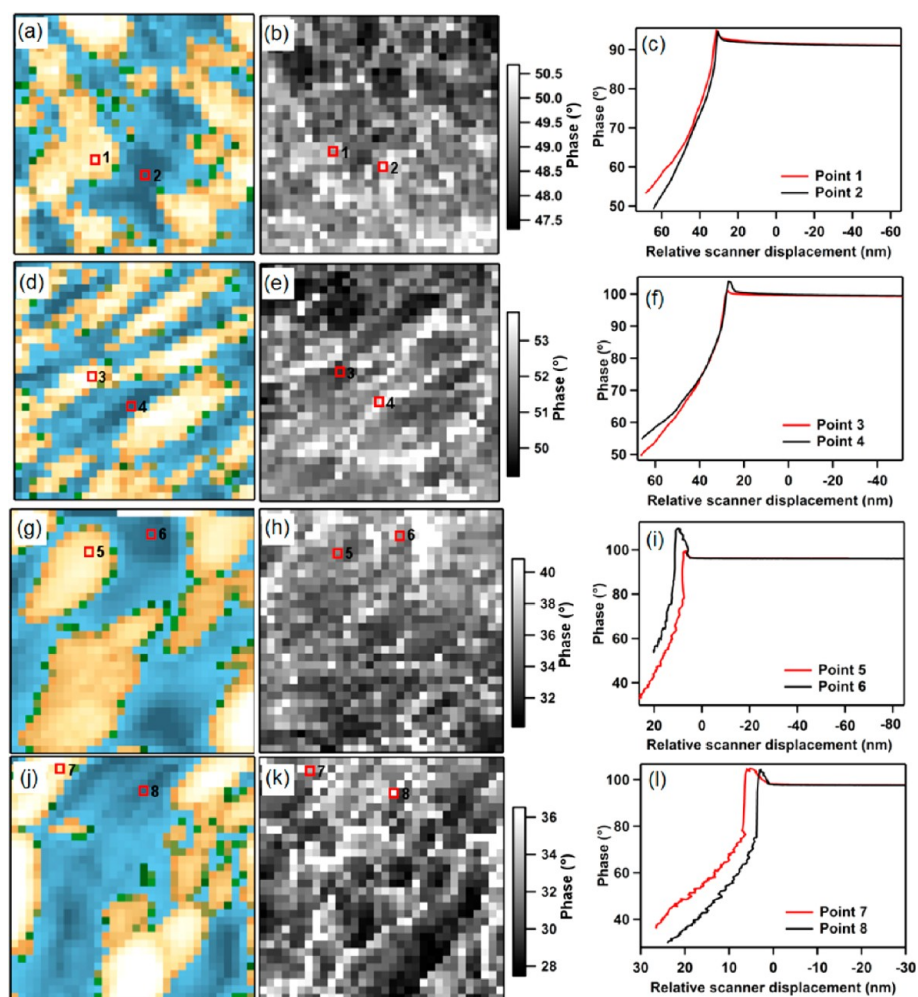

Figure 5. Examples of 500 nm phase-curve maps. Oxidized 2 mg/mL PPy/CS (a) topography (Z-scale 12 nm), (b) phase, (c) phase curves of points 1 and 2. Reduced 2 mg/mL PPy/CS (d) topography (Z-scale 10 nm), (e) phase, (f) phase curves of points 3 and 4. Oxidized 2 mg/mL PPy/HA (g) topography (Z-scale 60 nm), (h) phase, (i) phase curves of points 5 and 6. Reduced 2 mg/mL PPy/HA (j) topography (Z-scale 30 nm), (k) phase, (l) phase curves of points 7 and 8.

indicating that the tip remained in the attractive region. Therefore, the tip is not making contact with the surface in these regions and phase signal does not measure dissipative interactions associated with, for example, material stiffness. For the darker areas, the curves showed an initial small positive phase shift followed by a negative phase shift into the repulsive region. This was observed for both PPy/CS (Figure 3g) and PPy/HA (Figure 3h).

Collectively, the above observations indicate that the significant phase separation in both PPy/HA and PPy/CS generally occurs at the nodules versus the periphery of the nodules and that this is qualitatively well-defined in the AC mode phase images. Importantly, the phase maps and their phase-separation curves indicate that phase-separated regions showing a significant "jump" in the phase shift (e.g., from 100−120° down to 40−60°) are due to the tip differentially sampling attractive or repulsive interactions. A stronger, longer-range attractive interaction prevents the tip from entering the repulsive region over the nodule peripheries, while a weaker, shorter-range attractive interaction results in a shift to the repulsive region on the nodules.

Effect of Dopant Concentration. Further phase imaging was performed to assess the effect of varying dopant concentration on the phase-separated regions. Figure 4 shows representative phase images for each dopant concentration of PPy/CS (Figure 4a, 0.1 mg/mL; Figure 4b, 2 mg/mL; Figure 4c, 10 mg/mL) and PPy/HA (Figure 4d, 0.1 mg/mL; Figure 4e, 2 mg/mL; Figure 4f, 10 mg/mL). The magnitude of the phase difference between the phase-separated regions was observed to decrease with increasing dopant concentration, as indicated by the decreasing phase range of the scale bars (to the right of each image). The phase range for the scans of the samples was averaged and correlated with dopant concentration. A dopant concentration of 0.1 mg/mL had the highest difference with 56.7° ± 4.7° and 52.4° ± 0.9° for PPy/HA and PPy/CS, respectively. This decreased to 36.4° ± 3.2° and 23.3° ± 1.2° for a dopant concentration of 2 mg/mL and further reduced at the highest concentration of 10 mg/mL with 19.8° ± 2.3° and 12.8° ± 0.1°. The decrease in the phase difference was primarily due to a decrease in the positive phase shift, as phase values for the repulsive region generally remained constant. This indicated that the attractive interactions became weaker as dopant concentration increases. One important consideration was that changes in surface roughness of the films as function of the dopant concentration could also possibly influence the extent of the phase shifts. The average of the root-mean-square (rms) roughness values from several images for each dopant concentration are labeled in Figure 4. No significant change in roughness was observed as the dopant concentration was increased from 2 to 10 mg/mL; however, the magnitude of the phase shift decreased significantly for both films, indicating that roughness was not a causative factor at these higher dopant concentrations.

Effect of Electrical Stimulation. To exclude other possible causes such as topography for the differential sampling of attractive and repulsive forces, phase maps of PPy/CS and PPy/HA films were performed after oxidation and reduction. For PPy/CS, the topography image in the oxidized state (Figure 5a) showed clear nodules that were unchanged from the non-electrically stimulated films. The corresponding phase map (Figure 5b) showed some differences in the phase signal; however, the magnitude of the shift (as indicated by the scale bar) was significantly smaller in comparison to the non-

electrically stimulated films. These smaller phase shifts were confirmed in the corresponding phase-separation curves, which showed a similar profile for both the nodules (point 1) and nodule peripheries (point 2) (Figure 5c). Both phase curves showed a small positive shift before an overall negative shift (Figure 5c), indicating a significant reduction in the extent of the attractive branch on the nodule peripheries. Furthermore, we did not observe any phase-separation curves consisting of only purely attractive (branches) forces in all phase separation maps for both PPy/CS and PPy/HA, irrespective of oxidation or reduction. This was further emphasized when the maximum of the scale for all the phase maps was set to 90° (see Supporting Information Figure S2). Because no purely attractive regions, or phase values above 90°, were observed the contrast in these rescaled images is completely uniform with no phase separation. Therefore, the phase-separated regions were effectively removed by the oxidation and reduction even though the topography of the films did not significantly change, indicating that the latter is not the underlying cause of the phase separation observed in the non-electrically stimulated films. The phase value of each pixel in the maps is taken at the maximum point of the relative scanner displacement (i.e., minimum of tip−sample separation), and thus the phase contrast that still exists (Figure 5, parts b, e, h, k) is due to phase shifts only occurring in the repulsive branch, as shown by the phase-separation curves (Figure 5, parts c, f, i, l). This represents the situation where sampling of the phase (i.e., a deviation within the purely repulsive branch) can be related to the material stiffness. On the basis of the phase maps in Figure 5, the lighter (lower dissipation) and darker areas appeared to correlate with nodules and nodule peripheries, respectively, suggesting that the nodules are stiffer.

Kelvin Probe Force Microscopy. To correlate the phase separation with spatial variation in surface potential, KPFM was performed on the polymer films. Figure 6 shows the
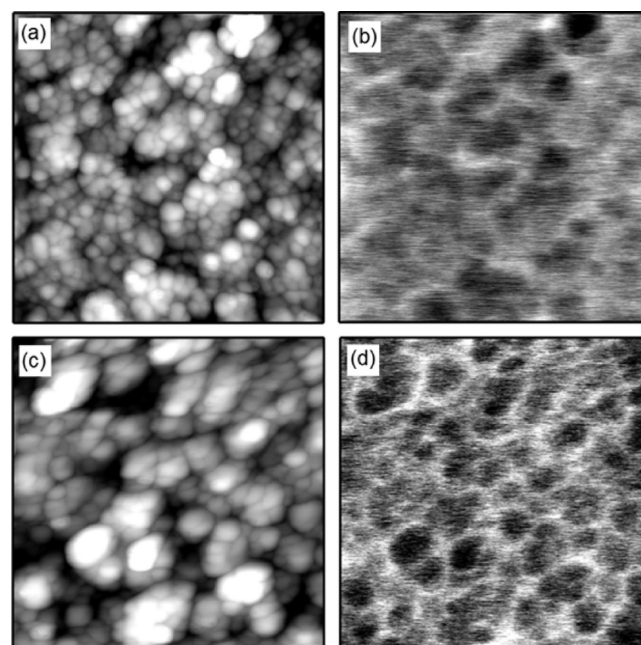

Figure 6. KPFM 1 μm scans of 2 mg/mL PPy/CS (a) topography and (b) surface potential; 2 mg/mL PPy/HA (c) topography and (d) surface potential. Z-scales 40 nm, 10 mV, 40 nm, and 10 mV, respectively.

topographical and corresponding KPFM scan of PPy/CS and PPy/HA films. For both polymers, the nodular structures correlate with a more negative surface potential (dark regions in Figure 6, parts b and d), while oppositely the peripheries around the nodules correlate with a more positive surface potential. Therefore, a clear spatial correlation exists between topography, attractive and repulsive phase-separated regions, and degree of surface potential.

■ DISCUSSION

AFM phase imaging has been used to shed light on the evolution of the polymerization process and inhomogeneity of conductivity in OCPs. O'Neil et al.[20,21] attributed phase separation in polybithiophene films to surface variations in the polymer stiffness, which further reflected amorphous or crystalline areas of the polymer. The phase-separated regions were described as being due to crystalline polymer forming the nodules in contrast to more amorphous polymer located at their periphery. For this to occur during electrochemical polymerization, higher molecular weight components were said to initially deposit to form the primary nuclei and proceed to eventually be the cores of the nodules. Smaller molecular weight components are then deposited later and become the nodule peripheries. The model described from this work suggests that because the higher molecular weight components are more likely to form crystalline polymer, then it is expected that the nodules have a higher stiffness.

The nomenclature for the phase signal in the above study is different to ours (i.e., our attractive branch of 180° = −90°; our repulsive branch of 0° = +90°); thus, one must not rely on directly comparing light and dark phase contrasts. For changes in modulus or viscoelasticity an increase in energy dissipated from the tip is observed as a shift from the purely repulsive branch of the phase (where the tip is intermittently contacting the sample). For example, a greater positive shift from 0° when the tip is in the repulsive region corresponds to areas of lower modulus. In the above study, this would correspond to a negative shift from +90° resulting in darker phase areas, as was observed at the nodule peripheries. We could arrive at the same conclusion if our images of the as-grown and non-electrically stimulated PPy/CS and PPy/HA were interpreted based only on the direction of the phase shift, i.e., a shift toward brighter phase regions at the nodule peripheries. However, by undertaking additional phase-separation curves further information reveals that the phase separation arises from variations in attractive and repulsive interactions between the tip and polymer. Our study closely follows previous work aimed at attempting to understand phase contrast by investigating Nafion membranes.[26] In this study, phase-curve maps of the Nafion consisted of two main types of phase−separation curves. One type of phase-separation curve required considerably more force to enter the repulsive region and was attributed to the C+ and H+ ion-rich regions that would damp the cantilever oscillation with an attractive electrostatic force at longer distances. A second type of curve moved quickly from the attractive to repulsive region with the final phase values indicating little energy dissipation. The interpretation of phase contrast related to attractive−repulsive transitions has also been specifically investigated in detail by others.[24,30]

Our results show that the phase separation in the non-electrically stimulated films arises from differences in the strength of attractive interactions across the polymer surface. These may be due to either variations in Coulombic forces or capillary forces, as discussed further below. Previous studies on polybithiophene films using conductive AFM have shown a higher conductivity in the nodules compared to the nodular periphery.[21] These observations are further supported by KPFM of as-grown PPy/para-toluene sulfonate films showing a more negative potential at the nodules,[31] indicating that these regions have a higher work function, or are more highly doped, than their peripheries. KPFM images of both the PPy/CS and PPy/HA films studied here in Figure 6 confirm these previous observations. For PPy doped with large, immobile polyelectrolytes such as CS and HA, there is often excess of these dopants, and electrochemical polymerization of the polymer can sometimes be difficult due to a prohibitive effect of the excess dopant on secondary growth. We commonly observed this effect (i.e., the film growth is inconsistent), particularly when attempting grow the polymers using higher dopant concentrations, which may suggest the presence of excess dopant surrounding more conductive regions of the polymer. These characteristics explains the previously reported poorly defined redox potentials and lower electroactivity of PPy/CS and PPy/HA films.[32]

It is possible that capillary forces may play a role in the phase separation.[33] Due to the preferential adsorption of water at hydrophilic regions, capillary neck formation and rupture between the tip and surface can lead to phase contrasts mechanisms. Simulated and experimental AFM observations show that the phase transition from the attractive to repulsive region is suppressed with an increase in relative humidity percent.[34,35] The presence of entrapped CS and HA in regions at the nodule peripheries may present a more hydrophilic surface (e.g., due to an excess of free anionic groups) that promotes greater adsorption of water layers under ambient conditions. This is in contrast to the regions where the CS and HA participate in charge neutrality. This effect may be exacerbated given that these polyelectrolytes, especially HA, are highly hydroscopic and their inclusion significantly increases the hydrophilicity of PPy films.[36] The one caveat here is that based on KPFM images the nodule peripheries generally show a more positive potential than the nodules, which does not correlate with the notion of excess anionic groups in the nodule peripheries. For the presence of Coulombic forces, it would follow that longer-range attractive interactions occur due to an electrostatic attraction between the tip, which carries a net negative charge,[37] and oppositely charged groups located at the nodule peripheries. The more negatively charged nodular regions observed in the KPFM images would conversely diminish the electrostatic attractive forces, leading to phase separation in the images. Oxidation and reduction of the polymers was shown to completely eliminate the phase-separated regions, a finding that may relate to charge redistribution and uniformity across the surface and/or increased charge neutrality via the incorporation of electrolyte ions (Na^+, $Cl^−$). Once the attractive force is removed by electrical stimulation, the smaller phase changes related to the material stiffness can be unveiled.

The inhomogeneous distribution of both dopants gives rise to nanometer spatial variations in surface chemistry and related nanoscale forces under the control of these regions. The observed variations in the strength of attractive forces represent differences in surface charge and/or surface energy that have implications for these materials when under investigation in a fluid, or biological, environment. For example, such surface variations may play a role in double-layer formation, which in

13504

dx.doi.org/10.1021/jp302944n | J. Phys. Chem. B 2012, 116, 13498–13505

turn can influence protein and cellular interactions. Further work is required to indeed understand the extent to which these variations in surface charge/energy will exert their influence over such biointeractions.

CONCLUSION

The observation of a striking phase separation that is not indicative of a change in the Young's modulus has led to details on the phase signal's relationship to variations in the surface charge and/or energy of the films. It is clear that when investigating heterogeneous polymers, such as the OCP studied here, AFM phase imaging is more clearly defined when the operating regime (i.e., attractive or repulsive) is established. Electrochemical oxidation and reduction can produce a more homogeneous surface chemistry, as evidenced by removal of the phase separation. The correlation between the nanoscale topography and variations in the spatial distribution of surface properties, including conductivity, degree of doping, and surface charge, also extends to fundamental surface forces that are yet to be directly measured in OCP. These lateral nanometer variations in surface forces may manifest in fluid and biological environments and have an influence on biointeractions such as protein and cell adhesion.

ASSOCIATED CONTENT

S **Supporting Information**

Height and phase maps with corresponding phase-separation curves from specific location in the maps of both PPy/CS and PP/HA films and phase maps after electrical stimulation of the films. This material is available free of charge via the Internet at http://pubs.acs.org.

AUTHOR INFORMATION

Corresponding Author

*E-mail: mhiggins@uow.edu.au (M.J.H.); gwallace@uow.edu.au (G.G.W.). Phone: +61-2-4221-3989 (M.J.H.); +61-2-4221-3127 (G.G.W.). Fax: +61-2-4221-3114 (M.J.H.); +61-2-4221-3114 (G.G.W.).

Notes

The authors declare no competing financial interest.

ACKNOWLEDGMENTS

REFERENCES

(1) Inzelt, G.; Pineri, M.; Schultze, J. W.; Vorotyntsev, M. A. *Electrochim. Acta* **2000**, *45*, 2403−2421.

(2) Rivers, T. J.; Hudson, T. W.; Schmidt, C. E. *Adv. Funct. Mater.* **2002**, *12*, 33−37.

(3) Cui, X.; Lee, V. A.; Yehoash, R.; Wiler, J. A.; Hetke, J. F.; Anderson, D. J.; Martin, D. C. *J. Biomed. Mater. Res.* **2001**, *56*, 261−272.

(4) Kim, D.-H.; Abidian, M.; Martin, D. C. *J. Biomed. Mater. Res., Part A* **2004**, *71A*, 577−585.

(5) Wallace, G. G.; Spinks, G. M.; Kane-Macguire, L. A. P.; Teasdale, P. R. *Conductive Electroactive Polymers*, 3rd ed.; CRC Press, 2009.

(6) Pernaut, J.-M.; Reynolds, J. R. *J. Phys. Chem. B* **2000**, *104*, 4080−4090.

(7) Wallace, G. G.; Moulton, S. E.; Clark, G. M. *Science* **2009**, *324*, 185−186.

(8) Garner, B.; Georgevitch, A.; Hodgson, A. J.; Lin, L.; Wallace, G. G. *J. Biomed. Mater. Res.* **1999**, *44*, 121−129.

(9) Collier, J. H.; Camp, J. P.; Hudson, T. W.; Schmidt, C. E. *J. Biomed. Mater. Res.* **2000**, *50*, 574−584.

(10) Moreno, J. S.; Panero, S.; Artico, M.; Filippini, P. *Bioelectrochemistry* **2008**, *72*, 3−9.

(11) Kotwal, A.; Schmidt, C. E. *Biomaterials* **2001**, *22*, 1055−1064.

(12) Schmidt, C. E.; Shastri, V. R.; Vacanti, J. P.; Langer, R. *Proc. Natl. Acad. Sci. U.S.A.* **1997**, *94*, 8948−8953.

(13) Guimard, N. K.; Gomez, N.; Schmidt, C. *Prog. Polym. Sci.* **2007**, *32*, 876−921.

(14) Lee, J. Y.; Schmidt, C. E. *Acta Biomater.* **2010**, *6*, 4396−4404.

(15) Gilmore, K. J.; Kita, M.; Han, Y.; Gelmi, A.; Higgins, M. J.; Moulton, S. E.; Clark, G. M.; Kapsa, R.; Wallace, G. G. *Biomaterials* **2009**, *29*, 5292−5304.

(16) Gelmi, A.; Higgins, M. J.; Wallace, G. G. *Biomaterials* **2010**, *31*, 1974−1983.

(17) Magonov, S. N.; Elings, V.; Whangbo, M.-H. *Surf. Sci.* **1997**, *375*, 385−391.

(18) Schmitz, I.; Schreiner, M.; Friedbacher, G.; Grasserbauer, M. *Appl. Surf. Sci.* **1997**, *115*, 190−198.

(19) Planes, J.; Samson, Y.; Cheguettine, Y. *Appl. Phys. Lett.* **1999**, *75*, 1395−1397.

(20) O'Neil, K. D.; Semenikhin, O. A. *J. Phys. Chem. C* **2007**, *111*, 14823−14832.

(21) O'Neil, K. D.; Shaw, B.; Semenikhin, O. A. *J. Phys. Chem. B* **2007**, *111*, 9253−9269.

(22) Semenikhin, O. A.; Jiang, L.; Iyoda, T.; Hashimoto, K.; Fujishima, A. *J. Phys. Chem. C* **1996**, *100*, 18603−18606.

(23) Semenikhin, O. A.; Jiang, L.; Hashimoto, K.; Fujishima, A. *Synth. Met.* **2000**, *110*, 115−122.

(24) Bar, G.; Thomann, Y.; Brandsch, R.; Cantow, H. J. *Langmuir* **1997**, *13*, 3807−3812.

(25) Magonov, S. N.; Cleveland, J.; Elings, V.; Denley, D.; Whangbo, M.-H. *Surf. Sci.* **1997**, *389*, 201−211.

(26) James, P. J.; Antognozzi, M.; Tamayo, J.; McMaster, T. J.; Newton, J. M.; Miles, M. J. *Langmuir* **2001**, *17*, 349−360.

(27) Cen, L.; Neoh, K. G.; Li, Y.; Kang, E. T. *Biomacromolecules* **2004**, *5*, 2238−2246.

(28) Moreno, J. S.; Panero, S.; Materazzi, S.; Martinelli, A.; Sabbieti, M. G.; Agas, D.; Materazzi, G. *J. Biomed. Mater. Res., Part A* **2009**, *88A*, 832−840.

(29) Magonov, S. N.; Elings, V.; Whangbo, M.-H. *Surf. Sci.* **1997**, *375*, 385−391.

(30) Chen, X.; Roberts, C. J.; Zhang, J.; Davies, M. C.; Tendler, S. J. B. *Surf. Sci.* **2002**, *519*, 593−598.

(31) Barisci, J. N.; Stella, R.; Spinks, G. M.; Wallace, G. G. *Electrochim. Acta* **2000**, *46*, 519−531.

(32) Thompson, B. C.; Moulton, S. E.; Richardson, R. T.; Wallace, G. G. *Biomaterials* **2011**, *15*, 3822−3831.

(33) Butt, H.-J.; Cappella, B.; Kappl, M. *Surf. Sci. Rep.* **2005**, *59*, 1−152.

(34) Zitzler, L.; Herminghaus, S.; Mugele, F. *Phys. Rev. B* **2002**, *66*, 155436.

(35) Schmitz, I.; Grasserbauer, M. *Appl. Surf. Sci.* **1997**, *115*, 190−198.

(36) Molino, P.; Higgins, M. J.; Innis, P. C.; Kapsa, R. M.; Wallace, G. G. *Langmuir* **2012**, *28*, 8433−8445.

(37) Laarz, E.; Meurk, A.; Yanez, J.; Bergstro, L. *J. Am. Ceram. Soc.* **2001**, *84*, 1675−1682.

13505

dx.doi.org/10.1021/jp302944n | *J. Phys. Chem. B* 2012, 116, 13498−13505